Acta Biomaterialia 190 (2024) 317–328

Contents lists available at ScienceDirect

Acta Biomaterialia

journal homepage: www.elsevier.com/locate/actbio

Full length article

Comparing continuum and direct fiber models of soft tissues: An ocular biomechanics example reveals that continuum models may artificially disrupt the strains at both the tissue and fiber levels

Xuehuan He [a], Mohammad R. Islam [a,c], Fengting Ji [a], Bingrui Wang [a], Ian A. Sigal [a,b,*]

[a] Department of Ophthalmology, University of Pittsburgh, Pittsburgh, PA, United States
[b] Department of Bioengineering, University of Pittsburgh, Pittsburgh, PA, United States
[c] Department of Mechanical Engineering, University of Texas Rio Grande Valley, Edinburg TX, United States

ARTICLE INFO

Keywords:
Collagen
Fiber
Eye
Optic nerve head
Sclera
Continuum mechanics
Fiber mechanics
Biomechanics
Finite element modeling

ABSTRACT

Collagen fibers are the main load-bearing component of soft tissues but difficult to incorporate into models. Whilst simplified homogenization models suffice for some applications, a thorough mechanistic understanding requires accurate prediction of fiber behavior, including both detailed fiber-level strains and long-distance transmission. Our goal was to compare the performance of a continuum model of the optic nerve head (ONH) built using conventional techniques with a fiber model we recently introduced which explicitly incorporates the complex 3D organization and interaction of collagen fiber bundles [1]. To ensure a fair comparison, we constructed the continuum model with identical geometrical, structural, and boundary specifications as for the fiber model. We found that: 1) although both models accurately matched the intraocular pressure (IOP)-induced globally averaged displacement responses observed in experiments, they diverged significantly in their ability to replicate specific 3D tissue-level strain patterns. Notably, the fiber model faithfully replicated the experimentally observed depth-dependent variability of radial strain, the ring-like pattern of meridional strain, and the radial pattern of circumferential strain, whereas the continuum model failed to do so; 2) the continuum model disrupted the strain transmission along each fiber, a feature captured well by the fiber model. These results demonstrate limitations of the conventional continuum models that rely on homogenization and affine deformation assumptions, which render them incapable of capturing some complex tissue-level and fiber-level deformations. Our results show that the strengths of explicit fiber modeling help capture intricate ONH biomechanics. They potentially also help modeling other fibrous tissues.

Statement of significance: Understanding the mechanics of fibrous tissues is crucial for advancing knowledge of various diseases. This study uses the ONH as a test case to compare conventional continuum models with fiber models that explicitly account for the complex fiber structure. We found that the fiber model captured better the biomechanical behaviors at both the tissue level and the fiber level. The insights gained from this study demonstrate the significant potential of fiber models to advance our understanding of not only glaucoma pathophysiology but also other conditions involving fibrous soft tissues. This can contribute to the development of therapeutic strategies across a wide range of applications.

1. Introduction

Glaucoma, a leading cause of irreversible blindness worldwide [2,3], is a progressive optic neuropathy characterized by optic disc excavation and the loss of retinal ganglion cell axons that transmit visual information from the eye to the brain [4,5]. Clinical and experimental evidence indicates that the initial site of injury in glaucoma is the ONH, in the posterior pole [6]. Elevated IOP is one of the main risk factors for glaucomatous neural tissue (NT) damage, and every current treatment is based on lowering IOP. The mechanisms by which IOP translates into NT damage remain unclear [7-9].

Understanding ONH sensitivity to IOP and thus individual

* Corresponding author at: Laboratory of Ocular Biomechanics, Department of Ophthalmology, University of Pittsburgh Medical Center, UPMC Mercy Pavilion, 1622 Locust Street, Rm 7.382, Pittsburgh, PA, United States 15219.
E-mail address: ian@ocularbiomechanics.com (I.A. Sigal).

https://doi.org/10.1016/j.actbio.2024.10.019
Received 23 August 2024; Received in revised form 30 September 2024; Accepted 15 October 2024
Available online 16 October 2024

susceptibility to glaucoma rests, in turn, in understanding how the tissues of the ONH region manage to bear biomechanical loads. Biomechanical support to the ONH region is provided by the collagenous connective tissues of the lamina cribrosa (LC) within the scleral canal, and the adjacent peripapillary sclera and the dura and pia maters [10]. The variability in individual susceptibility to IOP-related glaucomatous damage is thought to be due, at least in part, to differences in the mechanical behavior of the ONH tissues between individuals [11]. The desire to understand the sensitivity to IOP and susceptibility to glaucoma spurred the development of computational models that can capture the mechanical behavior of the tissues and the complex anatomy of the region. Early models simplified the tissues as linear, isotropic and homogeneous [12-17] or phenomenologically nonlinear [18]. Since collagen fibers are the primary load-bearing component of the ONH tissues, there has been great interest in developing computational models that can capture accurately the mechanical behavior of fibrous tissues. ONH models have thus advanced to incorporate inhomogeneous, anisotropic and nonlinear characteristics in some cases with fiber information derived from experiments [19-25].

Recent progress in imaging technology, specifically polarized light microscopy (PLM) [26-30] and its high speed variations [31,32], have enabled much improved visualization of the three-dimensional (3D) organization of collagen fiber bundles in the ONH [27,28,33]. Utilizing this detailed information, our research group has developed a direct fiber modeling framework that accounts for the complex 3D organization and continuity of the collagen fiber bundles as well as the interactions between fiber bundles, first for a small region of the sclera [34] and later for a wide region of the posterior pole incorporating the ONH, as shown in Fig. 1 [1].

The direct fiber modeling framework employed in this model can be seen as an alternative to the conventional continuum approaches which employ constitutive models that homogenize the fibers and assume affine kinematics between individual fibers and macroscopic tissue deformation [35], without accounting for fiber-fiber interactions. Elsewhere we have shown that ignoring interweaving and fiber-fiber interactions can introduce substantial errors when estimating sclera fiber mechanical properties using inverse fitting [36]. Continuum homogenized models, and even highly simplified phenomenological models have been proven sufficient to capture gross and generic mechanical behavior of the eye. However, a thorough mechanistic understanding of the ONH region requires accurate prediction of fiber behavior, including both detailed fiber-level strains and its long-distance transmission. Our goal in this study was to compare the performance of a continuum model of ONH built using conventional techniques with the fiber model which explicitly incorporates the complex 3D organization and interaction of collagen fiber bundles [1]. To ensure a fair comparison, we constructed the continuum model with identical geometrical, structural, and boundary specifications as for the fiber model.

Specifically, we considered the fiber structure-related parameters, such as fiber dispersion, volume fraction, and orientation, as heterogeneous across the domain in the continuum model, directly calculating them based on the fiber structure reconstructed in the fiber model. We identified other material parameters following an inverse modeling approach to match the model predictions with experimentally measured average displacements at 30mm Hg. The comparison began with comparisons between the models' predictions and experimental measures in terms of macro-level 3D tissue strain patterns and was followed by analyzing fiber-level long-distance strain transmission; corresponding results will be presented and discussed.

2. Methods

2.1. Continuum model geometry and boundary conditions

We constructed a continuum model that aimed to mirror the fiber model introduced in [1] and shown in Fig. 1, specifically in terms of geometries of the sclera, LC, NT, pia mater and dura mater as well as the boundary conditions (Fig. 2). The fiber model was constructed using PLM data obtained from cryosections of porcine ONH. It incorporates depth-dependent scleral fiber bundle distributions observed in PLM images, as well as longitudinal and circumferential fiber bundles in the pia mater and dura mater, effectively mirroring the complex three-dimensional organization of collagen structures observed histologically. The model represents individual fiber bundles through beam

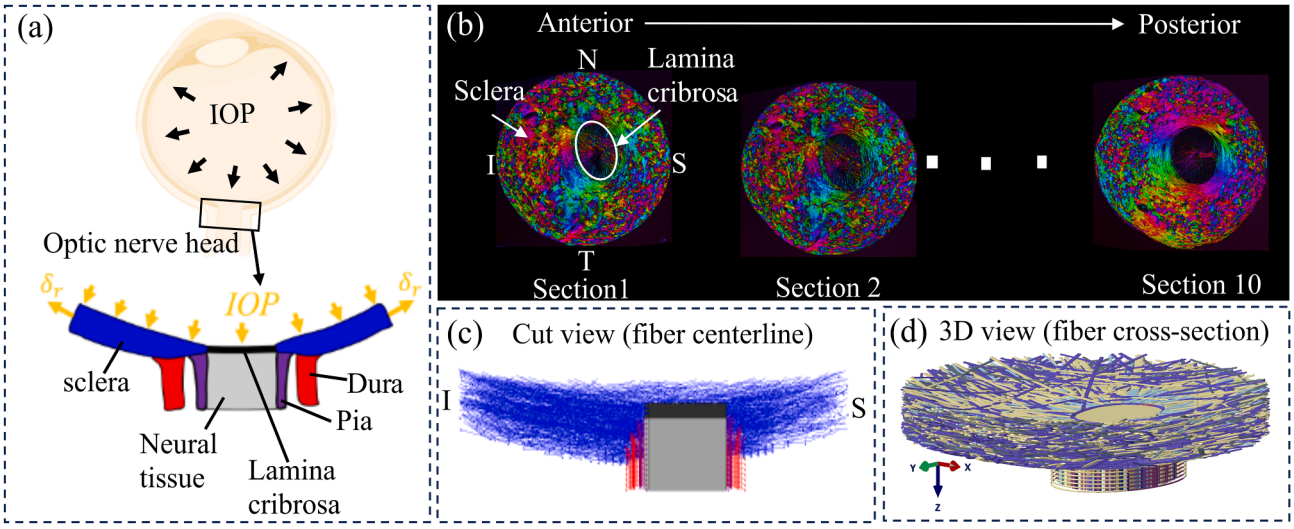

Fig. 1. Schematic of an eye cross-section with an enlarged view of posterior sclera (blue), LC (black), retrolaminar NT (grey), dura mater (red) and pia mater (purple) regions highlighted at the ONH. Boundary conditions included forces from IOP and displacements at the periphery. (b) Example images of serial coronal sections through the ONH of a pig eye from the anterior to posterior side. PLM was used to determine the collagen fiber orientation at each pixel [38]. Colors in the images indicate in-plane fiber orientation. Brightness indicates the strength of the signal. Low signal occurs when there is no birefringent material, no collagen, or the signal is blocked, for instance by pigment. The pig LC and scleral canal are elliptical with the major axis along the Nasal- Temporal (N-T) direction and the minor axis along the inferior-superior (I-S) direction. The Sections were stacked sequentially to construct a fiber model for modelling the collagenous tissues in the ONH region [1]. (c) Longitudinal cut-model view of the fiber model along the I-S direction with only bundle centerlines shown. (d) An isometric view of the complete fiber model with full bundle width displayed.

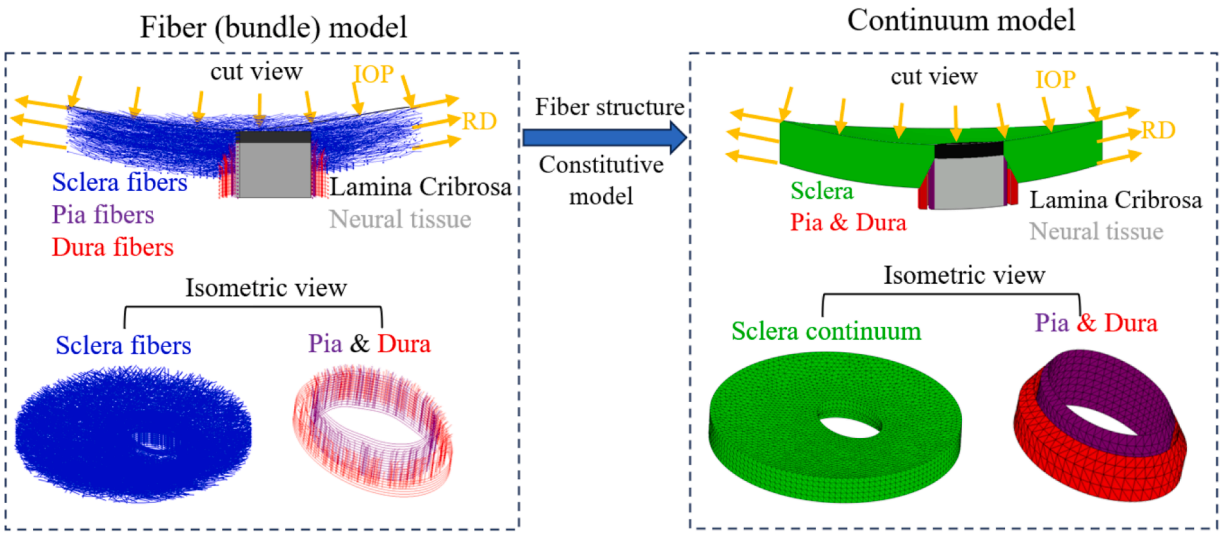

Fig. 2. Schematic illustration of the geometry and boundary conditions of the fiber model and the continuum models. The same boundary conditions were applied to both models to simulate an inflation experiment. The continuum model was meshed using quadratic 10-noded, tetrahedral mixed-formulation elements (C3D10H in Abaqus). A coarser mesh was selected for the peripheral sclera while a finer mesh was generated for the region where the peripapillary sclera, laminar cribrosa, neural tissue, pia mater and dura mater are located. After a mesh refinement analysis, it was decided that a mesh with ~78,000 elements and element size ranging from 0.1mm to 0.25mm was used for the simulation.

elements while treating the LC and NT as continuum structures. Readers interested in a more comprehensive description of the fiber model's construction, including the assumptions and their implications, should consult [1]. As illustrated in Fig. 2, both models were subjected to an elevated IOP of 30 mmHg. The same radial displacements (RD) used in the fiber model were applied to the continuum model's periphery to simulate the radial tension of the sclera due to IOP. Although our goal in this work focused on the mechanical behavior of the sclera, as it was in our previous papers [1,34,37], the continuum model incorporated a LC and retrolaminar NT. These provide a robust set of boundary conditions.

2.2. Continuum model material properties

The sclera, pia mater and dura mater in the continuum model were assumed to be incompressible, anisotropic, and heterogeneous. They were characterized using the Holzapfel-Gasser-Ogden (HGO) strain energy function [39]. The form of strain energy function, as implemented in ABAQUS, is given by:

$$W = W_{Ground} + W_{Fiber} \tag{1}$$

W is total strain energy density, W_{Fiber} is the strain energy density of the anisotropic collagen fibers and W_{Ground} is the isotropic strain energy density of the non-collagenous ground matrix.

The fiber strain energy density was modeled as:

$$W_{Fiber} = VF\frac{k_1}{2k_2}\sum_{\alpha=1}^{N}\left\{\exp\left[k_2\langle E_\alpha\rangle^2\right]-1\right\} \tag{2}$$

Where VF and $k_1$represents the volume fraction and elastic modulus of collagen fibers. k_2 is a material constant that governs how the stiffness of the fibers changes with the stretching of the fiber. N represents the number of fiber families.

The strain like quantity, E_α, is expressed as:

$$E_\alpha = \kappa(\overline{I}_1-3)+(1-3\kappa)(\overline{I}_4-1);\ \overline{I}_4 = M_\alpha\cdot\overline{C}M_\alpha \tag{3}$$

It represents the deformation of the fiber family with the mean direction, M_α, denoting as a 3D unit vector and the fiber angular dispersion, κ. Here, $\overline{C} = J^{-\frac{2}{3}}C$ is the modified right Cauchy-Green deformation tensor; and J is the determinant of the deformation gradient F. $\overline{I}_1$ is the first invariant of $\overline{C}$; and $\overline{I}_4$ is the squared stretches in the mean fiber direction, M_α. This model presumes that the orientation of the collagen fibers in each family is distributed rotationally symmetrically with respect to the mean preferred orientation $M(\theta,\phi)$. This rotational symmetry implies that the fiber orientation distribution is independent of the elevation angle ϕ, i.e., $\rho(M(\theta,\phi))\rightarrow\rho(\theta)$. The parameter, κ, is then defined as follows:

$$\kappa = \frac{1}{4}\int_0^{\pi}\rho(\theta)\sin^3(\theta)d\theta \tag{4}$$

The parameter κ takes values within the range [0, 1/3]. When $\kappa = 0$, fibers are completely aligned in the mean fiber direction (no dispersion). When $\kappa = 1/3$, the fibers are randomly distributed, and the material becomes isotropic.

The strain energy density equation for the ground material was modeled as a neo-Hookean solid in HGO model, which has the form:

$$W_{Ground} = (1-VF)C_{10}(\overline{I}_1-3)+\frac{1}{D}\left(\frac{(J^{el})^2-1}{2}-lnJ^{el}\right) \tag{5}$$

C_{10} is a material constant defining the stiffness of the ground substance. D value determines the compressibility of the material and is set to be 0 to account to for the incompressibility of the tissue. J^{el} is the elastic volume ratio.

The LC and NT regions were modeled as linear elastic material (ELC = 0.1 MPa, ENT = 0.01 MPa), same as the fiber model.

2.2.1. Identification of heterogeneous fiber dispersion, volume fraction and mean orientation

The fiber structure-related parameters of the HGO model, including fiber dispersion κ, fiber volume fraction v, and mean fiber direction M, were determined on an element-by-element basis based on the fiber structure of the fiber model reconstructed from 10 PLM images of porcine ONH coronal sections as shown in Fig. 1. To faithfully represent the heterogeneous fiber structural properties while maintaining the smoothness of material parameters in the tissue, in-house code was developed to calculate element-wise values of these three parameters. Briefly, for each element of the meshed sclera, pia and dura mater, neighboring elements whose center points are within 0.4mm—twice the

average element size—were selected along with this element as the region of interest (ROI). Fiber segments within the ROI were then extracted. The fiber volume fraction v was calculated as the ratio of the total fiber segments volume, considering the fiber bundle cross-section, to the total volume of the ROI. The direction vectors of the fiber segments were repeated in proportion to their relative volumes within the ROI. These direction vectors were then fitted to a 3D π-periodic von Mises distribution to obtain the mean fiber direction vector M and the

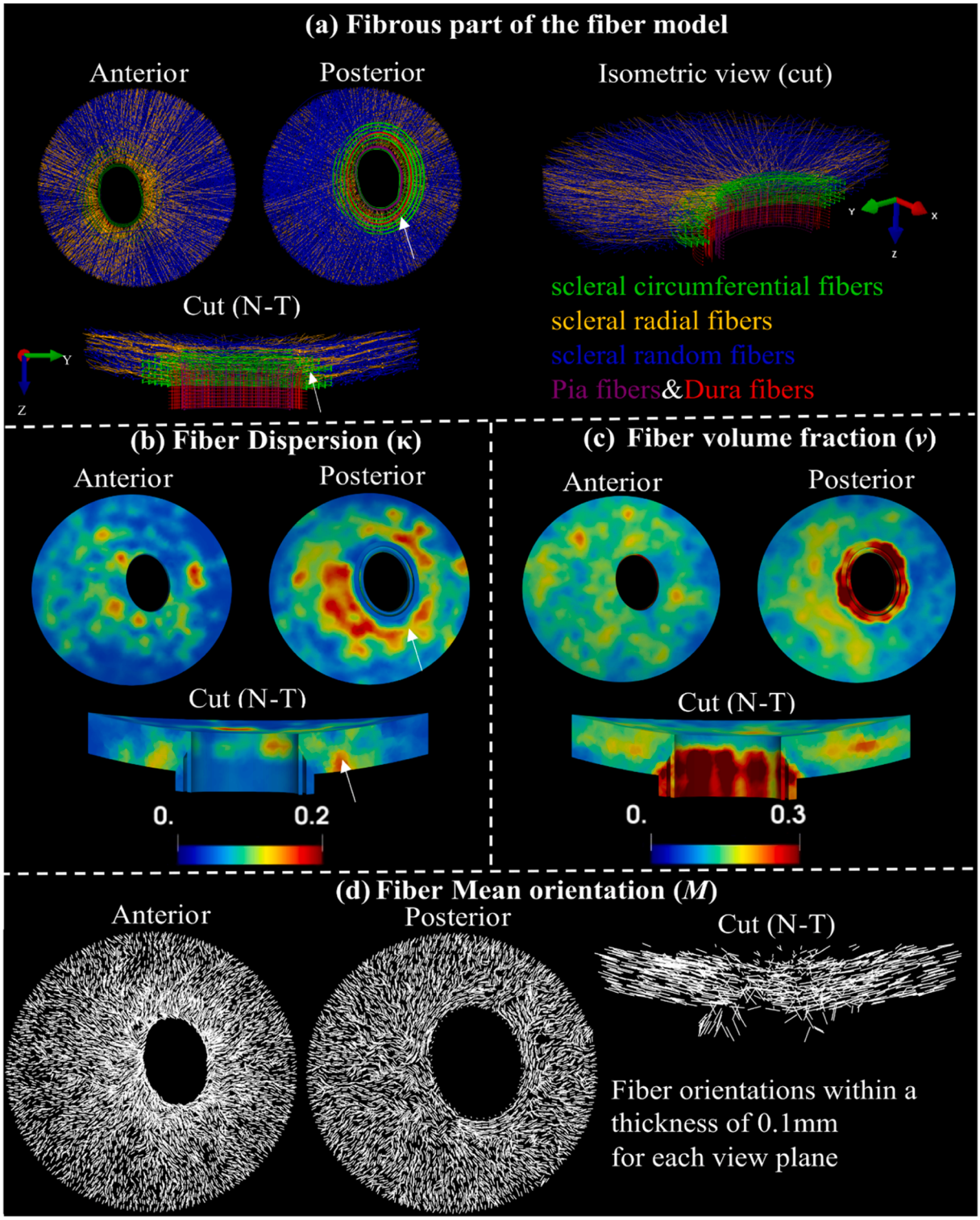

Fig. 3. Fiber structure and contours of structure parameters. Visualization of entire fibrous regions of the fiber model with scleral random (blue), scleral radial (orange), and scleral circumferential (green), pia (purple) and dura (red) fibers in anterior view, posterior view, a sectional and an isometric cut view along the nasal-temporal (N-T) direction (a). Maps of fiber dispersion (b), fiber volume fraction (c), and mean fiber orientation (c) for these fibrous regions in anterior, posterior, and the sectional cut views. Note that the fiber dispersion here is inversely related to its degree of anisotropy. The peripapillary scleral region (indicated by the white arrows) consists of green circumferential fibers and other types of fibers (a), indicating a highly dispersed or isotropic distribution of fibers in these regions, which is associated with higher fiber dispersion (b).

concentration parameter b. Because of the small element sizes in the continuum model, the fiber bundle orientations within an ROI were captured well by an orientation distribution function with a single fiber family (N=1). The fiber dispersion κ was then related to b as:

$$\kappa = \frac{1}{4}\int_0^{\pi} \rho(\theta,\ b)\sin^3(\theta)d\theta \tag{6}$$

Here, $\rho(\theta,\ b)$ is the 2D π-periodic von Mises distribution. The derived distributions of calculated fiber dispersion κ, fiber volume fraction v and mean fiber orientation M are shown in Fig. 3.

2.2.2. Identification of optimized matrix modulus, fiber modulus and exponential parameter

The other three HGO constitutive parameters, including the modulus of matrix C_{10}, modulus of fibers k_1, and the exponential parameter k_2 for fibers, were regarded as homogeneous across the tissue. These parameters were identified by inversely matching the IOP-induced posterior average displacement of the nerve region and peripapillary sclera (PPS), as well as average scleral canal expansion, with those derived from ex-vivo inflation experiments documented in the literature [40]. To determine optimized parameter values, a grid table formed by $C_{10} = [0.001 : 0.002 : 0.2]$ MPa, $k_1 = [20 : 10 : 200]$ MPa, $k_2 = [50 : 50 : 1000]$ was tested. The group of values that yielded the best match of simulated responses with the experimental data were regarded as the optimized parameter values. The finite element simulation was performed using the FE solver Abaqus/-Standard. Customized code and the GIBBON toolbox [41] for MATLAB v2023 [42] were used for model pre/post-processing and inverse identification of optimized parameters.

The simulation results of the continuum model with $C_{10} = 0.013$MPa, $k_1 = 120$ MPa and $k_2 = 500$ produced the best match with the experimental data in terms of posterior displacements of the nerve region and PPS as well as horizontal sclera expansion. Fig. 4 shows the predicted average displacements (dashed lines) with identified optimized material parameters of a porcine ONH from the fiber model (blue) and the continuum model (green) compared to the experimental measurements of different porcine eyes (circle symbols) obtained from ref.

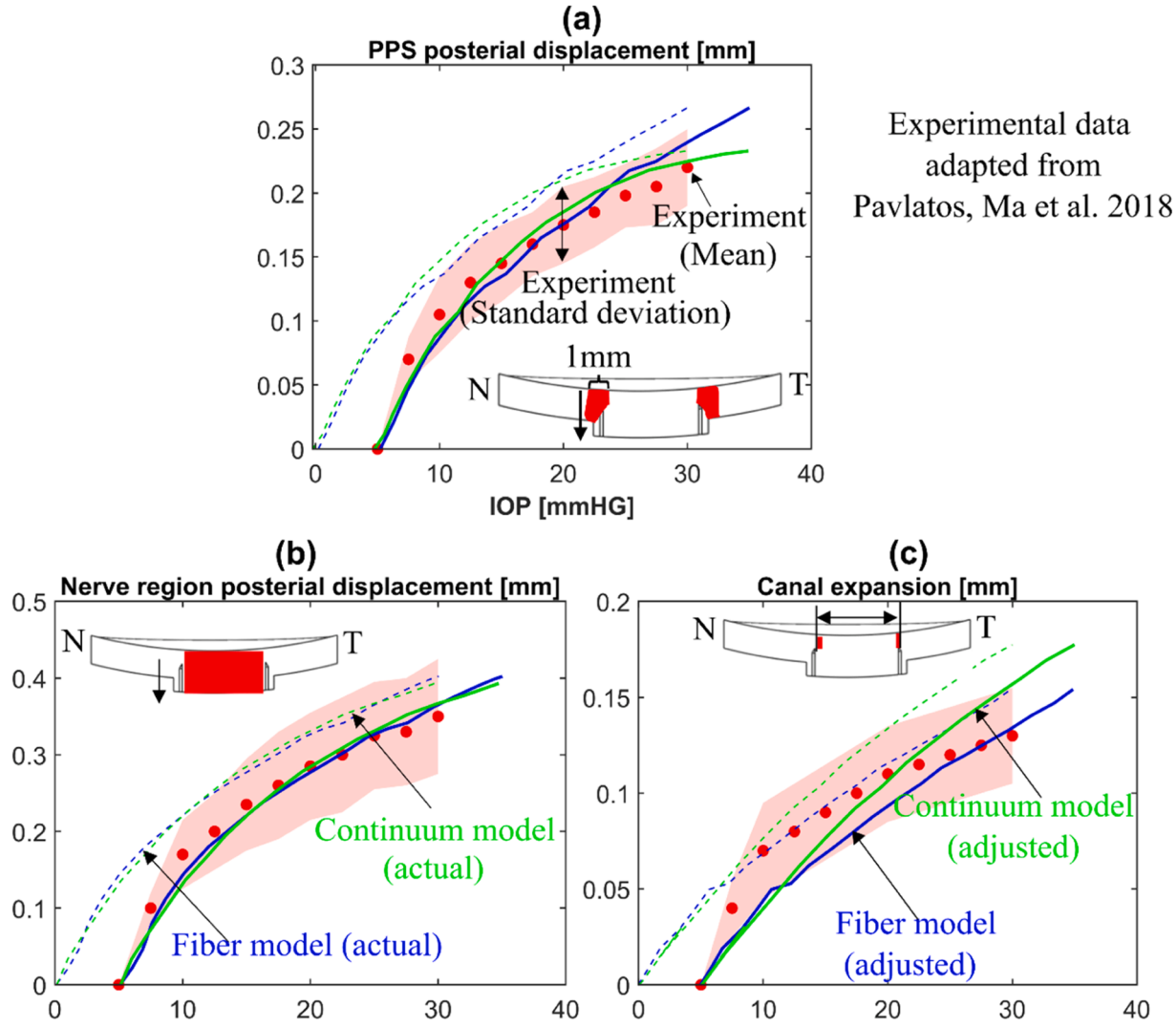

Fig. 4. Mechanical validation of the fiber (blue lines) and continuum(green lines) models. The comparisons of (a) the mean posterior displacement of the porcine peripapillary sclera (PPS), (b) the mean posterior displacement of the optic nerve region (LC and NT parts), and (c) the mean scleral canal expansion between the inflation experiments (circle symbols) from ref. [40] and the models (lines). Note that the specimen configurations at 5 mmHg were employed as the undeformed configuration for measuring ONH deformations in the experiments while the configuration at 0 mmHg was used as the undeformed configuration in the model. Therefore, the model responses are adjusted by 5 mm Hg in the IOP axis to account for differences in reference configurations. The shaded regions in (a)-(c) represent the standard deviation of experimental measurements for multiple porcine eyes (n = 12). The dashed and solid lines in (a)-(c) represent the actual and adjusted responses of the models, respectively. The insets in (a)-(c) indicate the regions used for calculating the mean posterior displacements and the canal expansion.

[40]. Note that the experimental displacements were measured over the ONH regions in the cross-section along the nasal-temporal (N-T) meridian direction. The same regions of the models were utilized to measure average model displacement. The shaded regions represent the standard deviation of experimental measurements from multiple eyes (n = 12). Albeit there is a slight difference of the response curves, the adjusted model predictions (solid lines) show excellent agreement with the experimental responses for all measurements. As expected, the actual model, without adjustment (dashed grey lines), does not match the experiments as well because of the difference in reference state. Please see the study introducing the fiber model for more on this topic [1].

2.3. Comparison of strains between the continuum and the fiber models

The displacement match in Fig. 4 served as a prerequisite for the subsequent comparison of strain patterns. The rationale behind this approach is that if the model intrinsically represents the tissue structure well, using optimized material properties derived from inversely matching the experimental displacement response, it should also match the experimental tissue strain patterns and reflect the fiber-level long-distance strain transmission behavior. As illustrated in Fig. 5, we calculated and compared both models in terms of the three-dimensional tissue-level strain patterns and fiber strains.

2.3.1. Comparisons of three-dimensional tissue strain patterns in sclera

Several studies have reported the tissue-level 3D strain patterns of the LC, NT, and sclera regions derived from experimental inflation tests [40,43-46]. We calculated the 3D tissue strains in the radial, circumferential, and meridional directions from the continuum and fiber models at 30 mm Hg, following the procedures illustrated in Fig. 5. In this study, we focused the comparison on the sclera region. The experimental strains reported for the sclera regions were derived from the human specimens [43,45],], whereas both models were constructed using data from a porcine specimen. While we developed a technique that allowed for reasonable comparison between the numerical models and experimental data, it is important to note that these data arise from fundamentally different types of analysis. Given these inherent differences, we concentrated on comparing the global strain patterns in the tissue rather than focusing on specific strain magnitudes. Our objective was not to determine which model could perfectly replicate the experimental results but to assess which model better captures the strain patterns on a broader scale.

For both models, the green strain tensor E at the centroid of each continuum element was calculated as $E = 0.5(F^T F - 1)$ where F is the deformation gradient tensor. For the continuum model, F was acquired directly from the simulation. For the fiber model, it was postprocessed based on the displacements of fiber nodes derived from the simulation. For each element's centroid in the continuum model, neighboring fiber nodes within 400um were selected and corresponding displacements vectors in the Cartesian coordinate were denoted as U_i $(i = x, y, z)$. The deformation gradient tensor F in the Cartesian coordinate was calculated as follows:

$$F = \begin{bmatrix} \frac{\partial U_x}{\partial x} + 1 & \frac{\partial U_x}{\partial y} & \frac{\partial U_x}{\partial z} \\ \frac{\partial U_y}{\partial x} & \frac{\partial U_y}{\partial y} + 1 & \frac{\partial U_y}{\partial z} \\ \frac{\partial U_z}{\partial x} & \frac{\partial U_z}{\partial y} & \frac{\partial U_z}{\partial z} + 1 \end{bmatrix} \tag{7}$$

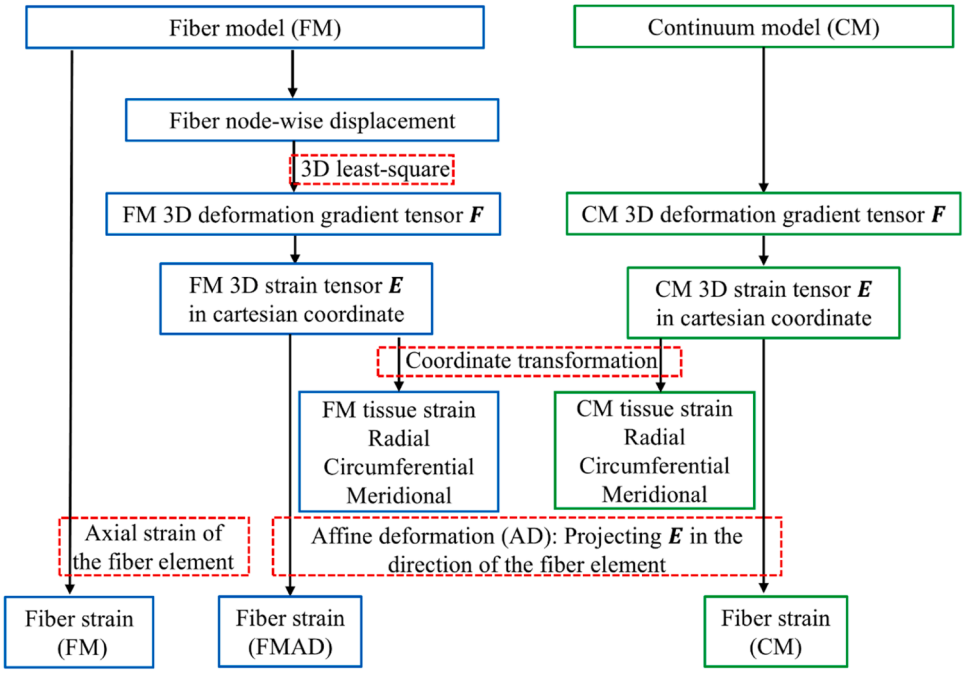

Fig. 5. A flowchart showing the procedures in deriving 3D tissue-level strains and fiber strains for the fiber (FM) and continuum (CM) models. The blue boxes correspond to steps and variables related to the FM, while the green boxes represent those for the CM. Red dashed boxes indicate specific methods or transformations employed, such as 3D least-squares fitting for the FM and coordinate transformation to spherical coordinates for both models. The deformation gradient tensor F in the CM was acquired directly from the simulation. For the FM, F was also calculated at the centroids of continuum elements based on nodal displacements to ensure consistent comparisons. The details of this calculation can be found in Section 2.3.1. Tissue-level strains in radial, circumferential and meridional directions were computed by transforming the strain tensor E from Cartesian coordinate to spherical coordinate, same as the approach utilized in acquiring the experimental tissue strain [43]. In the FM, fiber strain refers to the axial strain of the fiber element, derived directly from simulation results. For the CM, fiber strain was determined by projecting the 3D strain tensor $\boldsymbol{E}$ along the fiber element direction, following the affine deformation (AD) assumption commonly used in continuum kinematics [35]. This approach relies on the affine deformation (AD) assumption in the continuum kinematics. Employing the same AD assumption, fiber strain was also calculated based on the strain tensor derived from FM, and we refer this as the fiber strain for the fiber model with affine deformation (FMAD).

where the displacement gradients $\partial U_i/\partial U_j$ were obtained by a 3D least-squares method [47,48].

The derived Cartesian strain tensor E was transformed into spherical strain tensor E_{sph} in the spherical coordinate via a transformation matrix T as $E_{sph} = TET^T$ [46,49]. The T is given by:

$$T = \begin{bmatrix} sin\theta cos\varphi & sin\theta sin\varphi & cos\theta \\ cos\theta cos\varphi & cos\theta cos\varphi & -sin\theta \\ -sin\varphi & cos\varphi & 0 \end{bmatrix} \quad (8)$$

Where θ is the azimuth angle and φ is the elevational angle as shown in Fig. 6. The diagonal components of derived spherical strain tensor E_{sph} represent the normal strain in radial E_r, meridional E_φ and circumferential E_θ direction as denoted in Fig. 6, respectively.

2.4. Comparison of fiber strains between the continuum and fiber models

We followed the procedures depicted in Fig. 5 to calculate and compare fiber strains between the CM, FM, and FMAD at 30 mm Hg. This comparison focused on the distribution of fiber strains for fiber elements along each entire fiber in scleral fiber bundles. To quantify the degree of variation in fiber strains, we calculated the standard deviations of fiber strains along each entire fiber derived from the three models for all fibers

3. Results

3.1. Comparison of three-dimensional tissue strains between the continuum and fiber models

Predicted tissue-level radial strain patterns from the FM and CM were compared to experimentally measured patterns from a human eye [43] (Fig. 7). The experimentally measured radial strains exhibited depth-dependent variability from the anterior to the posterior side, with significant compression in the anterior, whereas the posterior side of the LC, NT and PPS were less compressed or even stretched. In addition to the study shown in Fig. 7a, this pattern has also been reported in another study for human sclera tissue [46]. The FM accurately replicated the depth-dependent variation of the radial strain for the PPS, whereas the CM did not. It is important to acknowledge that the LC and NT part, modeled as a continuum in both models, did not reproduce the experimental radial strain patterns.

The FM also replicated some interesting features of circumferential and meridional strain patterns observed experimentally from the posterior side of a human sclera [45], whereases the CM failed to (Fig. 8). Here, the circumferential strain seems to display a radial pattern, with bands emanating from the scleral canal and extending outward in all directions. In contrast, the meridional strain tends to follow a ring-like pattern, with large strains surrounding the scleral canal. The FM effectively captured these contrasting patterns and the pronounced near-canal meridional strains.

3.2. Comparison of fiber strains between the continuum and fiber models

The fiber strains derived from the FM, CM and FMAD for fiber elements along each entire fiber are shown in Fig. 9. Visually, the fiber strains in the FM appear quite smooth along each fiber but vary significantly in the CM and FMAD. This observation is further supported by the results of the standard deviations of fiber element strains along each fiber for all fibers, as shown in Fig. 10. Overall, the fiber strains exhibit a much lower degree of variation in the FM than in the CM and FMAD along each fiber.

4. Discussion

In this study, we employed the ONH as a test case to assess the biomechanical performance of our FM compared to a conventional CM developed using standard techniques. Our findings reveal that, while both models adequately matched the globally averaged displacement responses induced by IOP observed in experiments, they diverged dramatically in their ability to replicate specific 3D tissue-level strain patterns. Notably, the FM excelled in capturing the depth-dependent variability of radial strain, the ring-like pattern of meridional strain, and the radial pattern of circumferential strain —patterns which the CM failed to reproduce. Moreover, the FM preserved the smooth strain transmission along each fiber, in contrast to the conventional CM, which disrupted this transmission. Below, we discuss the motivation and rationale for the study as well as the significance of each finding.

Collagen fibers are the main load-bearing component of soft tissues but difficult to incorporate into models. Conventional CMs represent the collagenous fibers in soft tissues as homogenized continuum structures, which are effective for predicting macro-scale responses but lack the capacity to provide detailed fiber-level behaviors necessary to fully comprehend fibrous tissue biomechanics [22,24,45,50]. To overcome these shortcomings, we have developed a FM that explicitly incorporates the complex 3D organization and interactions of collagen fiber bundles within the ONH. The motivation for this research is to highlight the significant advantages of our fiber model over conventional continuum models. By using the ONH as a test case, we aim to demonstrate that our model can more accurately predict both the intricate tissue-level strain patterns and the long-distance strain transmission along the fibers, which are crucial for advancing our understanding of fibrous tissue

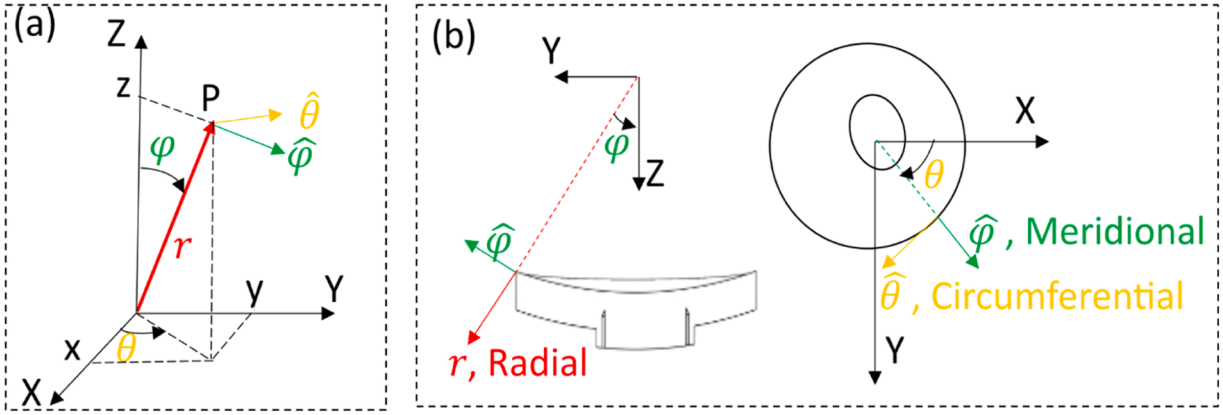

Fig. 6. (a): Schematic of the 3D cartesian coordinate (X, Y, Z) and spherical coordinate (r, θ, φ) systems. (b): Illustration of the radial, meridional and circumferential directions for the ONH model in cut view (N-T direction) and anterior view. The radial direction was defined to be aligned with the through-thickness direction of the ONH, which agrees with the experimental data.

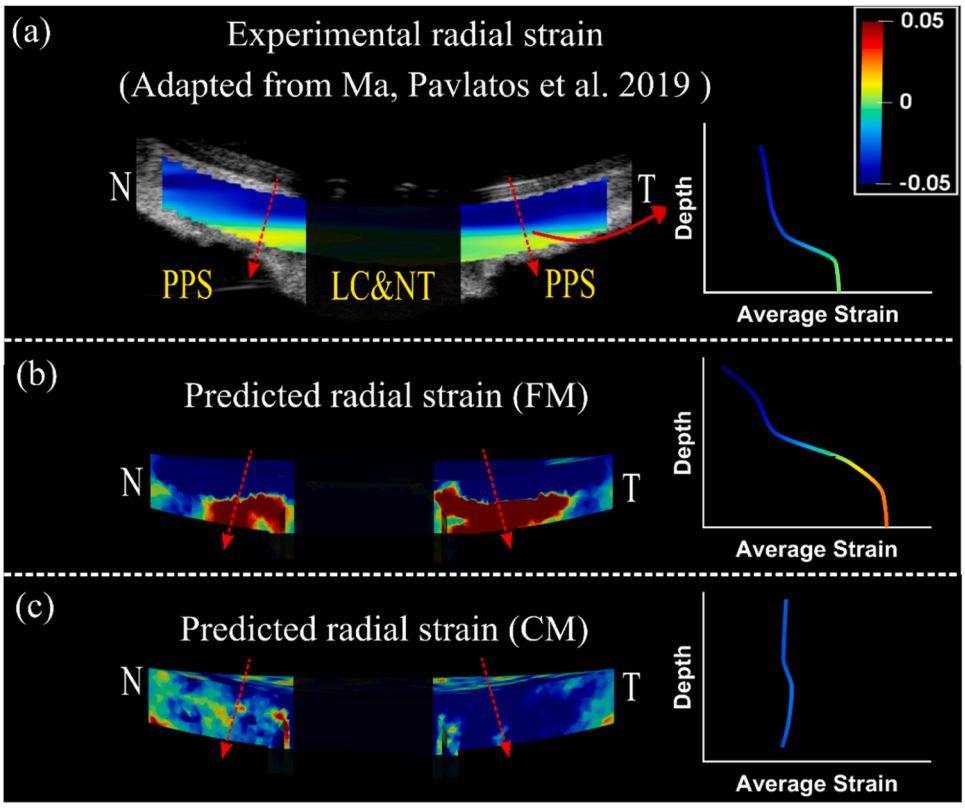

Fig. 7. A comparison of the experimental (a) [43], the FM predicted (b) and the CM predicted (c) radial strains for the sclera region in the sagittal section of the ONH along the Nasal-Temporal (NT) direction at 30 mm Hg. The red arrows indicate the direction of radial strain at through-thickness points, represented by corresponding dashed lines, which are oriented from anterior to posterior. The detailed direction convention can also be found in Fig. 6. The sagittal region was divided into ten layers of equal thickness along the through-thickness direction, with the average radial strain calculated for each layer and plotted against the depth. The experimental data show a depth-dependent, step-function variation in strain, with greater compression at the anterior and lesser compression or extension at the posterior. Note that the fiber model reflected this variation pattern, but the continuum model failed to reflect it.

biomechanics and linking tissue biomechanics with cellular mechanobiology [51].

We acknowledge that the models we compare are distinct, by nature, and therefore that there will always be differences between them. Nevertheless, we contend that the comparison between them is fair, for the following reasons: Both models were developed with identical geometric and boundary specifications, ensuring a level basis for comparison When it comes to material properties, the two models account for the properties of the same fiber structure but intrinsically diverge in their approaches to representing it. The FM accurately reconstructed the fiber structure, assigning a linear stiffness to each fiber bundle. In contrast, the CM simplifies the fiber structure into a homogenized continuum and employs an anisotropic, structurally motivated constitutive model to account for the material properties. In this constitutive model, fiber structure-related parameters—such as volume fraction, dispersion, and mean orientation were directly calculated and assigned to each mesh element based on the detailed fiber structure used in the fiber model. For each element, the region of interest (ROI) is defined as twice the average element size to ensure inclusion of surrounding elements. This approach guarantees the smoothness of the material domain and replicates the local structural properties as accurately as possible. Other material parameters, including the modulus of the matrix and fibers, and the exponential parameter, were assumed to be homogeneous across the domain. These parameters were inversely identified by matching the model predictions with experimentally measured responses. It is important to note that the assumption of homogeneity for these parameters is not arbitrary but follows standard practice in these types of studies [19,21,23]. Furthermore, unlike previous studies that typically rely on estimated parameter values from prior research, our study enhances the accuracy and relevance of our models by employing an optimization process through inverse modeling, aligning with the method used in determining fiber stiffness for the FM [1]. However, it is crucial to recognize that despite our efforts to align the models as closely as possible, the two approaches remain inherently distinct. No modeling approach can perfectly replicate another due to fundamental differences. Thus, while our efforts ensure a fair comparison, they also highlight the unique contributions and limitations inherent in each modeling approach.

Our results demonstrated that both models performed equally well in replicating the experimentally measured nonlinear IOP-induced average displacement responses of the ONH through an inverse modeling approach, with one parameter optimized for the FM and three for the CM (Fig. 4). However, significant differences emerged when it came to capturing 3D tissue-level strain patterns in the sclera region. The FM, despite using only one parameter to represent the linear, isotropic fiber bundles modeled as beams, was able to capture both the nonlinear IOP-induced mean displacement responses of the ONH and the 3D strain patterns in the sclera. In contrast, although the CM employed six constitutive parameters and could replicate the nonlinear displacement responses, it failed to capture the 3D strain patterns of the sclera. Previous studies [40,44] have also reported similar depth-dependent radial strain patterns in the porcine LC and NT, showing significant anterior compression and posterior stretching. This raises the possibility that if the fibrous structures of the LC and NT tissue were also explicitly modeled, similar accurate results could be achieved for these regions. Further, studies have reported that the average meridional strain in the porcine ONH is greater than the circumferential strain [46,52,53]. This finding is consistent with the results from the FM, which showed a larger

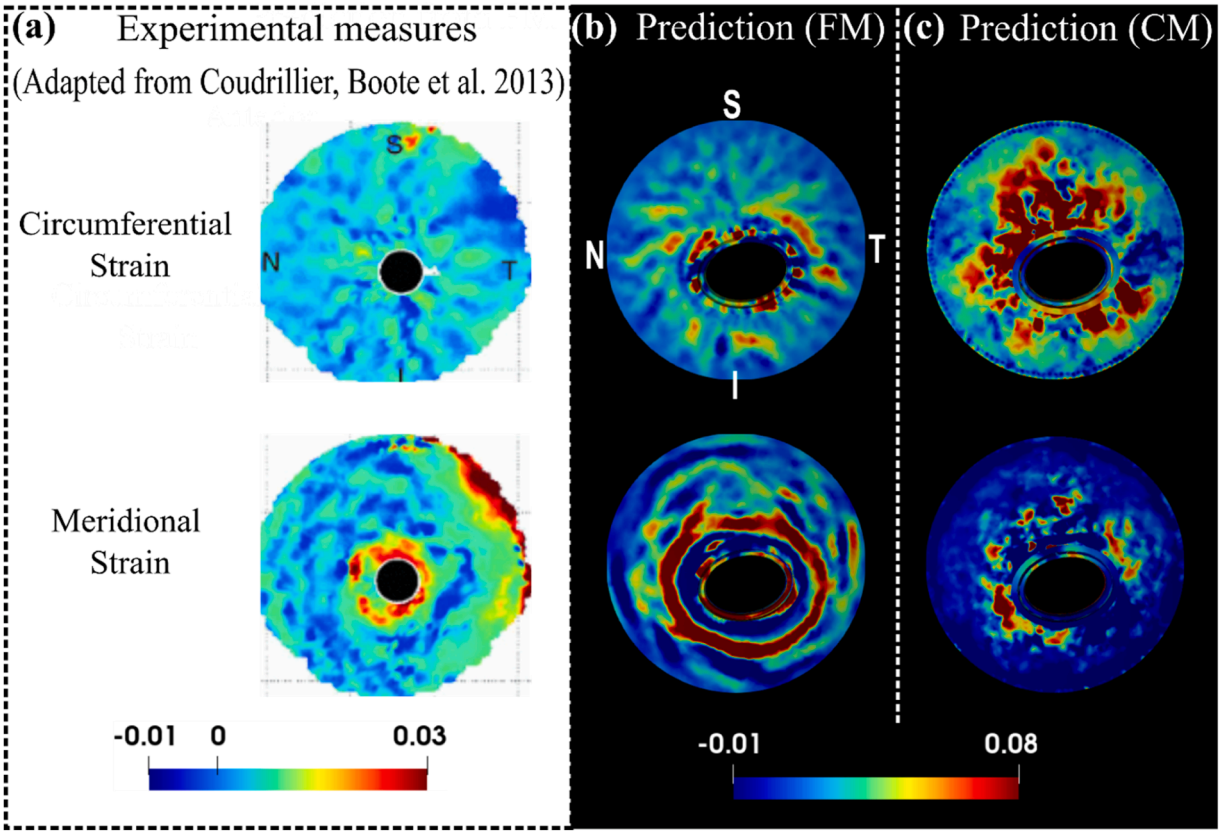

Fig. 8. A comparison of the experimental (a), the FM predicted (b) and the CM predicted (c) circumferential and meridional scleral strain patterns from the posterior view of the ONH at 30 mm Hg. Detailed direction conventions for the circumferential and meridional strains are described in Fig. 6. The plots of model predictions (b and c) were adjusted to align with the experimental plots in terms of the positions of the four quadrants: nasal (N), temporal (T), superior (S), and inferior (I). The experimental patterns, derived from a human sclera specimen [45], interestingly show contrasting global strain behaviors: the circumferential strain radiates from the sclera canal, forming a pattern with outward-extending bands, whereas the meridional strain appears as a series of open, ring-shaped bands with high values concentrated near the canal. These contrasting global patterns and pronounced near-canal meridional strains were captured by the fiber model but not by the continuum model.

average meridional strain of 0.089 compared to an average circumferential strain of 0.0265. In contrast, the CM indicated more pronounced stretching in the circumferential direction, with average meridional and circumferential strains of 0.017 and 0.042, respectively. This can also be observed in Fig. 8. However, we have not highlighted this finding as a main result of our study because it is derived from just one specimen. Nevertheless, it underscores the potential of the FM. These findings highlight that while the CM is effective for modeling large-scale tissue displacements, it is limited in its ability to represent complex 3D deformation patterns. Conversely, the FM shows considerable promise in capturing these detailed strain patterns, emphasizing its potential to provide a more accurate representation of biomechanical behavior in fibrous tissues.

In the second stage of our comparison, we focused on strain transmission along each fiber. The FM allows for direct visualization of fiber kinematics and consistently demonstrated smooth strain distribution along each fiber, as evidenced in Fig. 9. In contrast, the CM exhibited substantial variation in fiber strain (Figs. 9 and 10) due to its inherent kinematic assumptions. To address concerns that the observed "unsmoothness" or variation in fiber strain within the CM was due to discrepancies in tissue-level strain distributions between the continuum and FMs, we introduced the FM with affine deformation (FMAD). This model recalculated fiber strain using the same affine deformation assumption typically applied in continuum kinematics but based the calculation on the 3D strain tensor derived directly from the FM. This approach ensures that the observed strain "unsmoothness" is not merely a result of differences in the macro-level strain distributions between the models. However, even when FMAD was employed to calculate the fiber strain, the "unsmoothness" remained significant, as illustrated in Figs. 9 and 10. This persistence of variation suggests that the issue extends beyond simple alignment of tissue-level strains and points to fundamental limitations of the affine deformation assumptions in continuum kinematics. This finding demonstrates the reliability of the FM and underscores the need for a thorough evaluation of the CM's ability to link macroscopic tissue responses with cellular and sub-cellular level activities.

We recognize the substantial expertise within the field dedicated to advancing CMs of fibrous soft tissues. To bridge the gap between macroscopic observations and microscale behavior, multiscale CMs based on representative volume elements (RVEs) have been developed [54]. These models diverge from traditional constitutive material models by accounting for fiber-fiber interactions and non-affine deformations, as detailed in [55-57]. The RVE technique employs a two-scale sequential strategy, homogenizing the microscale behavior of discrete RVEs to derive the macroscale CM response. Each RVE, representing a small patch of networked fibers, influences the behavior at every integration point of the broader CM. Although innovative, the RVE method has limitations, especially due to its reliance on the continuum framework, such as the assumption of fiber independence among elements, which prevents fibers from crossing element boundaries or interacting with fibers within adjacent elements. Additionally, the homogeneous loading of RVE faces with displacements derived directly from the macroscopic solution implies an affine assumption for fiber displacements at the boundary, potentially oversimplifying the complex

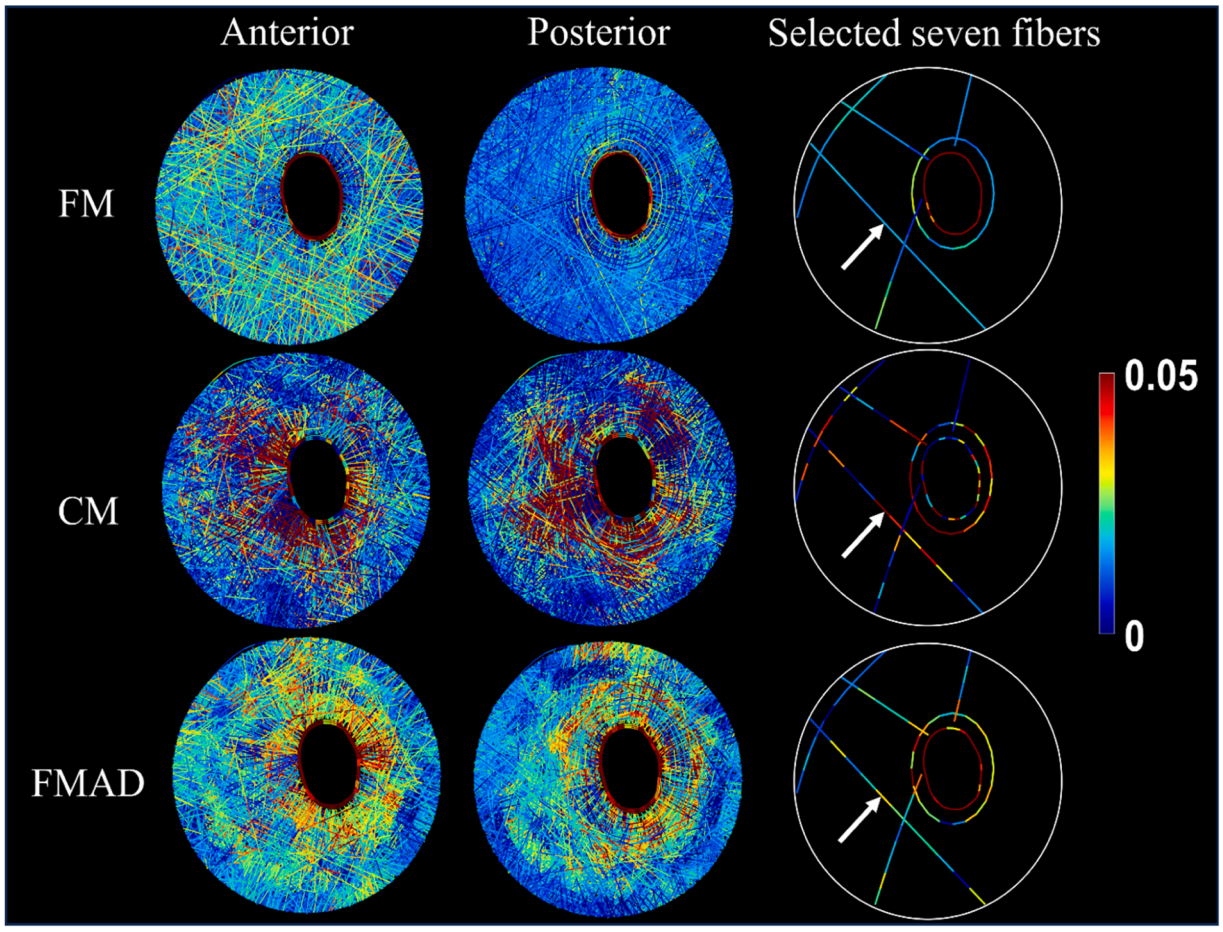

Fig. 9. Visualization of fiber strains for all sclera fibers (anterior view in the first column and posterior view in the second column) and seven selected whole fibers (third columns) in FM, CM, and FMAD. The selection of seven fibers allows for a clearer investigation of the fiber strain changes along each fiber. Further information on the fiber strain calculation methodologies for each model can be found in Fig. 5 and Section 2.3.1. Take the fiber indicated by the arrows as an example. Note how the smooth strains along the fiber in the FM were disrupted in the CM and FMAD due to the enforcement of affine deformation in calculating the fiber strains. Interestingly, the fiber strains within the FM exhibit depth-dependent variation, with larger strains evident in the anterior view and smaller strains in the posterior view. This variation appears to be less pronounced or absent in the CM and FMAD models.

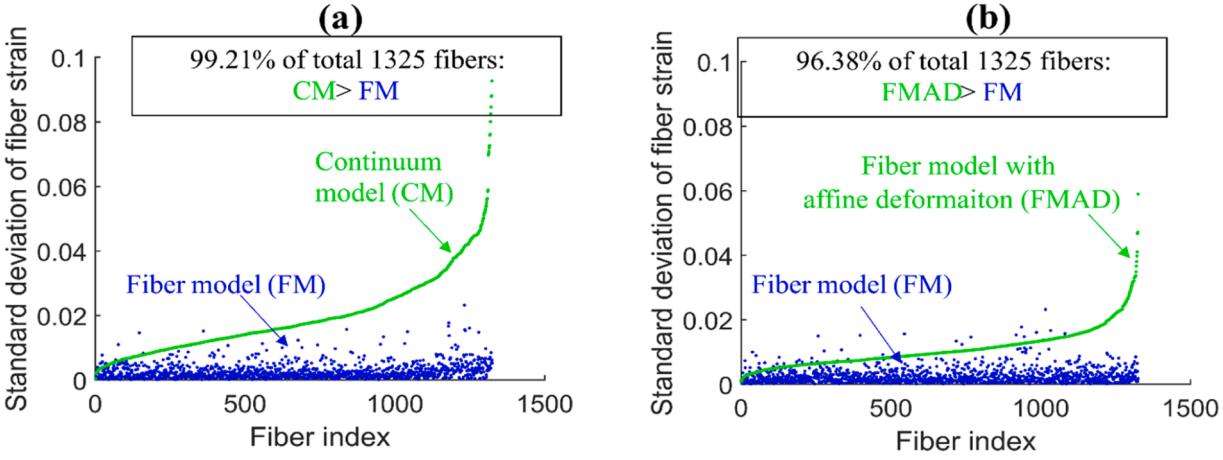

Fig. 10. Scatterplots of the standard deviations of fiber element strains along each of the 1325 fibers derived from CM and FM in (a) and from FMAD and FM in (b). Fibers are indexed according to the standard deviation of fiber strains from the CM in (a) and FMAD in (b). The plots highlight that fiber strains from FM are notably consistent along each fiber (low standard deviations), with 97% of fibers from FM exhibiting standard deviations below 0.01.whereas those calculated enforcing affine deformation in continuum kinematics (CM and FMAD) show significantly more variability.

structures and kinematics of real tissues. Therefore, despite advancements made by the RVE method, its intrinsic limitations associated with the continuum framework persist, and we believe that the FM outperforms it, particularly in accurately capturing detailed fiber kinematics and long-range strain transmission in fibrous tissues.

It is important to acknowledge several limitations in this study. Firstly, the two models were constructed using data from a single porcine eye specimen, while the experimental 3D strain patterns for the sclera were derived from human eyes (see Figs. 7 and 8). However, consistent depth-dependent step function variations in the radial strain patterns of the LC and NT have been reported in both porcine and human specimens, with porcine specimens showing a significantly greater magnitude of anterior compression and posterior stretching [40,43,44,46]. Additionally, human specimens exhibit similar depth-dependent strain patterns in the LC, NT, and sclera [40,44]. Therefore, we hypothesize that both human and porcine sclera display similar strain patterns, with individual specimen differences likely affecting strain magnitudes more than the patterns themselves. This study focused on comparing the strain patterns rather than absolute values, reinforcing the relevance of the results despite the use of different species.

Secondly, as previously mentioned in the manuscript, the modulus of fiber, matrix, and the exponential parameters were assumed to be homogeneous throughout the fibrous region and were inversely identified. Assigning heterogeneous properties might improve the match of strain patterns in CM; however, the current settings already provide a good approximation of global displacement. If we considered these parameters as heterogeneous, defining a suitable distribution of them across the domain would be challenging. Additionally, the inverse fitting process would become extremely complicated, computationally expensive, and difficult to achieve unique solutions based on the currently used IOP-average displacement response. It remains unknown whether using experimentally measured deformation patterns as objectives for inverse modeling would succeed in accurately determining heterogeneous mechanical properties. However, even if such a match were achieved, it would mean that the CM requires much more complex inverse modeling and more material parameters than the FM to match the 3D strain patterns. Moreover, as discussed previously in the manuscript, matching macroscopic strain patterns does not resolve the 'unsmoothness' of fiber strains under the affine deformation assumption.

Thirdly, the incompressibility assumption commonly used in modeling ONH [13,19,21,22,58-61], and other soft tissues [62-65] has been widely acknowledged. However, experiments have shown that the ONH and sclera exhibit volumetric compression under inflation [46,66,67], suggesting a reconsideration of this assumption. Compressibility of the tissue in the simulations could be achieved through tuning the parameter D. However, this would significantly increase the computational burden. It is still unclear whether assuming compressibility would improve the match of strain patterns.

Fourthly, the LC and NT are currently modeled as a homogenized continuum with linear and isotropic material properties in both models. It is important to clarify that our intent in this study, and in [1], was to focus on the fibrous structure and mechanics of the sclera. The tissues of the canal, namely the LC and NT, were incorporated solely to ensure that the sclera was modeled with reasonable boundary conditions. Therefore, we were satisfied to model them as continuum structures with linear elastic materials. We acknowledge that this is not typically the case, and most studies in the literature tend to focus on the LC while using the sclera for boundary conditions. However, we are not the first to take the opposite approach [68]. Our emphasis on the sclera is also why we believe it is appropriate to direct our attention to the sclera when comparing our model predictions with experimental results. Additionally, although the sclera was modeled as anisotropic and non-homogeneous in the CM, this approach did not successfully match the experimental strain patterns. Given these outcomes, we suspect that modeling the LC and NT as a continuum with anisotropic and heterogeneous properties could potentially yield more precise results on the behavior of these tissues. Moreover, as discussed elsewhere in the manuscript, we believe that explicitly modeling the fibrous structures of tissues in the LC and NT, similar to the sclera fibers in the FM, could lead to greater accuracy.

In conclusion, using the ONH as a test case, the FM demonstrates significant advantages over the CM in modeling fibrous tissues, particularly in its ability to accurately capture intricate 3D strain patterns and fiber kinematics, which are essential for understanding tissue biomechanics. While the FM has its limitations—such as the use of representative collagen fiber density, exclusion of the hydrated matrix, and assumptions about frictionless interactions and fiber crimp—it still represents a critical step forward in advancing biomechanical modeling. These limitations, as discussed in detail in the paper [1], provide opportunities for future refinement. Despite these challenges, we believe the insights from our study underscore FM's potential and, more ambitiously, its necessity for further development. This model holds promise for studying the biomechanics and mechanobiology of the ONH and other fibrous soft tissue.

Funding

Supported in part by National Institutes of Health R01-EY023966, T32-EY017271, P30-EY008098, Eye and Ear Foundation (Pittsburgh, PA), Research to Prevent Blindness (unrestricted grant to UPMC's Department of Ophthalmology and Stein Innovation Award to IA Sigal).

CRediT authorship contribution statement

Xuehuan He: Writing – review & editing, Writing – original draft, Visualization, Validation, Software, Methodology, Formal analysis, Data curation, Conceptualization. **Mohammad R. Islam:** Validation, Software, Formal analysis, Data curation. **Fengting Ji:** Software, Methodology, Data curation. **Bingrui Wang:** Methodology, Conceptualization. **Ian A. Sigal:** Writing – review & editing, Supervision, Software, Resources, Project administration, Methodology, Investigation, Funding acquisition, Formal analysis, Data curation, Conceptualization.

Declaration of competing interest

The authors declare that they have no known competing financial interests or personal relationships that could have appeared to influence the work reported in this paper.

References

[1] M.R. Islam, F. Ji, M. Bansal, Y. Hua, I.A. Sigal, Fibrous finite element modeling of the optic nerve head region, Acta Biomater. 175 (2024) 123–137.
[2] S. Resnikoff, D. Pascolini, D. Etya'ale, I. Kocur, R. Pararajasegaram, G.P. Pokharel, S.P. Mariotti, Global data on visual impairment in the year 2002, Bull. World Health Organ. 82 (11) (2004) 844–851.
[3] Y.C. Tham, X. Li, T.Y. Wong, H.A. Quigley, T. Aung, C.Y. Cheng, Global Prevalence of Glaucoma and Projections of Glaucoma Burden through 2040: A Systematic Review and Meta-Analysis, Ophthalmology. 121 (11) (2014) 2081–2090.
[4] G.R. Howell, I. Soto, R.T. Libby, S.W. John, Intrinsic axonal degeneration pathways are critical for glaucomatous damage, Exp. Neurol. 246 (2013) 54–61.
[5] R.W. Nickells, G.R. Howell, I. Soto, S.W. John, Under pressure: cellular and molecular responses during glaucoma, a common neurodegeneration with axonopathy, Annu Rev. Neurosci. 35 (2012) 153–179.
[6] H.A. Quigley, E.M. Addicks, W.R. Green, A.E. Maumenee, Optic nerve damage in human glaucoma. II. The site of injury and susceptibility to damage, Arch. Ophthalmol. 99 (4) (1981) 635–649.
[7] H.A. Quigley, Glaucoma: Macrocosm to Microcosm The Friedenwald Lecture, Invest. Ophthalmol. Vis. Sci. 46 (8) (2005) 2663–2670.
[8] I.A. Sigal, R.A. Bilonick, L. Kagemann, G. Wollstein, H. Ishikawa, J.S. Schuman, J. L. Grimm, The Optic Nerve Head as a Robust Biomechanical System, Invest. Ophthalmol. Vis. Sci. 53 (6) (2012) 2658–2667.
[9] Z. Zhu, S. Waxman, B. Wang, J. Wallace, S.E. Schmitt, E. Tyler-Kabara, H. Ishikawa, J.S. Schuman, M.A. Smith, G. Wollstein, I.A. Sigal, Interplay between intraocular and intracranial pressure effects on the optic nerve head in vivo, Exp. Eye Res. 213 (2021) 108809.

[10] J.C. Downs, M.D. Roberts, I.A. Sigal, Glaucomatous cupping of the lamina cribrosa: a review of the evidence for active progressive remodeling as a mechanism, Exp. Eye Res. 93 (2) (2011) 133–140.
[11] I.A. Sigal, J.G. Flanagan, C.R. Ethier, Factors Influencing Optic Nerve Head Biomechanics, Invest. Ophthalmol. Vis. Sci. 46 (11) (2005) 4189–4199.
[12] A.J. Bellezza, R.T. Hart, C.F. Burgoyne, The optic nerve head as a biomechanical structure: initial finite element modeling, Invest. Ophthalmol. Vis. Sci. 41 (10) (2000) 2991–3000.
[13] I.A. Sigal, J.G. Flanagan, I. Tertinegg, C.R. Ethier, Predicted extension, compression and shearing of optic nerve head tissues, Exp. Eye Res. 85 (3) (2007) 312–322.
[14] I.A. Sigal, J.G. Flanagan, I. Tertinegg, C.R. Ethier, Modeling individual-specific human optic nerve head biomechanics. Part II: influence of material properties, Biomech. Model. Mechanobiol. 8 (2) (2009) 99–109.
[15] I.A. Sigal, J.G. Flanagan, I. Tertinegg, C.R. Ethier, Modeling individual-specific human optic nerve head biomechanics. Part I: IOP-induced deformations and influence of geometry, Biomech. Model. Mechanobiol. 8 (2) (2009) 85–98.
[16] I.A. Sigal, H. Yang, M.D. Roberts, C.F. Burgoyne, J.C. Downs, IOP-induced lamina cribrosa displacement and scleral canal expansion: an analysis of factor interactions using parameterized eye-specific models, Invest. Ophthalmol. Vis. Sci. 52 (3) (2011) 1896–1907.
[17] I.A. Sigal, H. Yang, M.D. Roberts, J.C. Downs, Morphing methods to parameterize specimen-specific finite element model geometries, J. Biomech. 43 (2) (2010) 254–262.
[18] S.L.Y. Woo, A.S. Kobayashi, W.A. Schlegel, C. Lawrence, Nonlinear material properties of intact cornea and sclera, Exp. Eye Res. 14 (1) (1972) 29–39.
[19] R. Grytz, K. Krishnan, R. Whitley, V. Libertiaux, I.A. Sigal, C.A. Girkin, J.C. Downs, A mesh-free approach to incorporate complex anisotropic and heterogeneous material properties into eye-specific finite element models, Comput. Methods Appl. Mech. Eng. 358 (2020) 112654.
[20] R. Grytz, G. Meschke, J.B. Jonas, The collagen fibril architecture in the lamina cribrosa and peripapillary sclera predicted by a computational remodeling approach, Biomech. Model. Mechanobiol. 10 (3) (2011) 371–382.
[21] A. Karimi, R. Grytz, S.M. Rahmati, C.A. Girkin, J.C. Downs, Analysis of the effects of finite element type within a 3D biomechanical model of a human optic nerve head and posterior pole, Comput. Methods Programs Biomed. 198 (2021) 105794.
[22] A. Karimi, S.M. Rahmati, R. Razaghi, C.A. Girkin, J.Crawford Downs, Finite element modeling of the complex anisotropic mechanical behavior of the human sclera and pia mater, Comput. Methods Programs Biomed. 215 (2022) 106618.
[23] A.P. Voorhees, N.J. Jan, I.A. Sigal, Effects of collagen microstructure and material properties on the deformation of the neural tissues of the lamina cribrosa, Acta Biomater. 58 (2017) 278–290.
[24] L. Zhang, J. Albon, H. Jones, C.L.M. Gouget, C.R. Ethier, J.C.H. Goh, M.J.A. Girard, Collagen Microstructural Factors Influencing Optic Nerve Head Biomechanics, Invest. Ophthalmol. Vis. Sci. 56 (3) (2015) 2031–2042.
[25] H.G. Kollech, A. Ayyalasomayajula, R. Behkam, E. Tamimi, K. Furdella, M. Drewry, J.P. Vande Geest, A Subdomain Method for Mapping the Heterogeneous Mechanical Properties of the Human Posterior Sclera, Front. Bioeng. Biotechnol. 7 (2019) 129.
[26] A. Gogola, N.J. Jan, B. Brazile, P. Lam, K.L. Lathrop, K.C. Chan, I.A. Sigal, Spatial Patterns and Age-Related Changes of the Collagen Crimp in the Human Cornea and Sclera, Invest. Ophthalmol. Vis. Sci. 59 (7) (2018) 2987–2998.
[27] A. Gogola, N.J. Jan, K.L. Lathrop, I.A. Sigal, Radial and Circumferential Collagen Fibers Are a Feature of the Peripapillary Sclera of Human, Monkey, Pig, Cow, Goat, and Sheep, Invest. Ophthalmol. Vis. Sci. 59 (12) (2018) 4763–4774.
[28] N.J. Jan, K. Lathrop, I.A. Sigal, Collagen Architecture of the Posterior Pole: High-Resolution Wide Field of View Visualization and Analysis Using Polarized Light Microscopy, Invest. Ophthalmol. Vis. Sci. 58 (2) (2017) 735–744.
[29] B. Yang, B. Brazile, N.J. Jan, Y. Hua, J. Wei, I.A. Sigal, Structured polarized light microscopy for collagen fiber structure and orientation quantification in thick ocular tissues, J. Biomed. Opt. 23 (10) (2018) 1–10.
[30] B. Yang, N.J. Jan, B. Brazile, A. Voorhees, K.L. Lathrop, I.A. Sigal, Polarized light microscopy for 3-dimensional mapping of collagen fiber architecture in ocular tissues, J. Biophotonics. 11 (8) (2018) e201700356.
[31] P.Y. Lee, H. Schilpp, N. Naylor, S.C. Watkins, B. Yang, I.A. Sigal, Instant polarized light microscopy pi (IPOLπ) for quantitative imaging of collagen architecture and dynamics in ocular tissues, Opt. Lasers. Eng. 166 (2023) 107594.
[32] P.Y. Lee, B. Yang, Y. Hua, S. Waxman, Z. Zhu, F. Ji, I.A. Sigal, Real-time imaging of optic nerve head collagen microstructure and biomechanics using instant polarized light microscopy, Exp. Eye Res. 217 (2022) 108967.
[33] F. Ji, M. Quinn, Y. Hua, P.Y. Lee, I.A. Sigal, 2D or not 2D? Mapping the in-depth inclination of the collagen fibers of the corneoscleral shell, Exp. Eye Res. 237 (2023) 109701.
[34] F. Ji, M. Bansal, B. Wang, Y. Hua, M.R. Islam, F. Matuschke, M. Axer, I.A. Sigal, A direct fiber approach to model sclera collagen architecture and biomechanics, Exp. Eye Res. 232 (2023) 109510.
[35] Y. Lanir, Multi-scale Structural Modeling of Soft Tissues Mechanics and Mechanobiology, Journal of Elasticity 129 (1) (2017) 7–48.
[36] B. Wang, Y. Hua, B.L. Brazile, B. Yang, I.A. Sigal, Collagen fiber interweaving is central to sclera stiffness, Acta Biomater. 113 (2020) 429–437.
[37] A.P. Voorhees, N.J. Jan, Y. Hua, B. Yang, I.A. Sigal, Peripapillary sclera architecture revisited: A tangential fiber model and its biomechanical implications, Acta Biomater. 79 (2018) 113–122.
[38] N.J. Jan, J.L. Grimm, H. Tran, K.L. Lathrop, G. Wollstein, R.A. Bilonick, H. Ishikawa, L. Kagemann, J.S. Schuman, I.A. Sigal, Polarization microscopy for characterizing fiber orientation of ocular tissues, Biomed. Opt. Express. 6 (12) (2015) 4705–4718.
[39] T.C. Gasser, R.W. Ogden, G.A. Holzapfel, Hyperelastic modelling of arterial layers with distributed collagen fibre orientations, J. R. Soc. Interface 3 (6) (2006) 15–35.
[40] E. Pavlatos, Y. Ma, K. Clayson, X.J. Pan, J. Liu, Regional Deformation of the Optic Nerve Head and Peripapillary Sclera During IOP Elevation, Invest. Ophthalmol. Vis. Sci. 59 (2018) 3779–3788.
[41] K.M. Moerman, The Geometry and Image-Based Bioengineering Add-On, The Journal of Source Software 3 (2018) 506.
[42] T.M. Inc, MATLAB version: 9.13.0 (R2022b), The MathWorks Inc., The MathWorks Inc., Natick, Massachusetts, 2022.
[43] Y. Ma, E. Pavlatos, K. Clayson, X. Pan, S. Kwok, T. Sandwisch, J. Liu, Mechanical Deformation of Human Optic Nerve Head and Peripapillary Tissue in Response to Acute IOP Elevation, Invest. Ophthalmol. Vis. Sci. 60 (4) (2019) 913–920.
[44] E. Pavlatos, X. Pan, R.T. Hart, P.A. Weber, J. Liu, ONH Deformation in Porcine Eyes Using Ultrasound Speckle Tracking, Invest. Ophthalmol. Vis. Sci. 57 (12) (2016), 3568-3568.
[45] B. Coudrillier, C. Boote, H.A. Quigley, T.D. Nguyen, Scleral anisotropy and its effects on the mechanical response of the optic nerve head, Biomech. Model. Mechanobiol. 12 (5) (2013) 941–963.
[46] S. Kwok, Y. Ma, X. Pan, J. Liu, Three-Dimensional Ultrasound Elastography Detects Age-Related Increase in Anterior Peripapillary Sclera and Optic Nerve Head Compression During IOP Elevation, Invest. Ophthalmol. Vis. Sci. 64 (7) (2023) 16.
[47] F. Kallel, J. Ophir, A Least-Squares Strain Estimator for Elastography, Ultrason. ImAging 19 (3) (1997) 195–208.
[48] Y. Ma, E. Pavlatos, K. Clayson, S. Kwok, X. Pan, J. Liu, Three-Dimensional Inflation Response of Porcine Optic Nerve Head Using High-Frequency Ultrasound Elastography, J. Biomech. Eng. 142 (5) (2020) 0510131–0510137.
[49] L. Anand, S. Govindjee, Continuum Mechanics of Solids, Oxford University Press, 2020.
[50] S.A. Schwaner, B.G. Hannon, A.J. Feola, C.R. Ethier, Biomechanical properties of the rat sclera obtained with inverse finite element modeling, Biomech. Model. Mechanobiol. 19 (6) (2020) 2195–2212.
[51] J.D. Humphrey, E.R. Dufresne, M.A. Schwartz, Mechanotransduction and extracellular matrix homeostasis, Nat. Rev. Mol. Cell Biol. 15 (12) (2014) 802–812.
[52] B. Coudrillier, J. Tian, S. Alexander, K.M. Myers, H.A. Quigley, T.D. Nguyen, Biomechanics of the Human Posterior Sclera: Age- and Glaucoma-Related Changes Measured Using Inflation Testing, Investigative Opthalmology & Visual Science 53 (4) (2012).
[53] K.M. Myers, B. Coudrillier, B.L. Boyce, T.D. Nguyen, The inflation response of the posterior bovine sclera, Acta Biomater. 6 (11) (2010) 4327–4335.
[54] M. Dalbosco, T.A. Carniel, E.A. Fancello, G.A. Holzapfel, Multiscale numerical analyses of arterial tissue with embedded elements in the finite strain regime, Comput. Methods Appl. Mech. Eng. 381 (2021) 113844.
[55] B. Agoram, V.H. Barocas, Coupled macroscopic and microscopic scale modeling of fibrillar tissues and tissue equivalents, J. Biomech. Eng. 123 (4) (2001) 362–369.
[56] P.L. Chandran, V.H. Barocas, Deterministic material-based averaging theory model of collagen gel micromechanics, J. Biomech. Eng. 129 (2) (2007) 137–147.
[57] T. Stylianopoulos, V.H. Barocas, Volume-averaging theory for the study of the mechanics of collagen networks, Comput. Methods Appl. Mech. Eng. 196 (31) (2007) 2981–2990.
[58] C. Boote, I.A. Sigal, R. Grytz, Y. Hua, T.D. Nguyen, M.J.A. Girard, Scleral structure and biomechanics, Prog. Retin. Eye Res. 74 (2020) 100773.
[59] I.C. Campbell, S. Lovald, M. Garcia, B. Coudrillier, Biomechanical Properties of the Sclera, in: I. Pallikaris, M.K. Tsilimbaris, A.I. Dastiridou (Eds.), Ocular Rigidity, Biomechanics and Hydrodynamics of the Eye, Springer International Publishing, Cham, 2021, pp. 77–105.
[60] B. Coudrillier, C. Boote, H.A. Quigley, T.D. Nguyen, Scleral anisotropy and its effects on the mechanical response of the optic nerve head, Biomech. Model. Mechanobiol. 12 (5) (2013) 941–963.
[61] R.E. Norman, J.G. Flanagan, I.A. Sigal, S.M.K. Rausch, I. Tertinegg, C.R. Ethier, Finite element modeling of the human sclera: Influence on optic nerve head biomechanics and connections with glaucoma, Exp. Eye Res. 93 (1) (2011) 4–12.
[62] J.M. Guccione, A.D. McCulloch, L.K. Waldman, Passive material properties of intact ventricular myocardium determined from a cylindrical model, J. Biomech. Eng. 113 (1) (1991) 42–55.
[63] X. He, J. Lu, Explicit consideration of fiber recruitment in vascular constitutive formulation using beta functions, J. Mech. Phys. Solids. 163 (2022) 104837.
[64] X. He, J. Lu, Modeling planar response of vascular tissues using quadratic functions of effective strain, Int. J. Numer. Method. Biomed. Eng. 39 (4) (2023) e3653.
[65] G.A. Holzapfel, T.C. Gasser, R.W. Ogden, A New Constitutive Framework for Arterial Wall Mechanics and a Comparative Study of Material Models, Journal of elasticity and the physical science of solids 61 (1) (2000) 1–48.
[66] B. Coudrillier, D.M. Geraldes, N.T. Vo, R. Atwood, C. Reinhard, I.C. Campbell, Y. Raji, J. Albon, R.L. Abel, C.R. Ethier, Phase-Contrast Micro-Computed Tomography Measurements of the Intraocular Pressure-Induced Deformation of the Porcine Lamina Cribrosa, IEEe Trans. Med. ImAging 35 (4) (2016) 988–999.
[67] X. Jia, F. Zhang, M. Cao, Z. Pan, K. Liu, D. Zhou, X. Duan, Elevated IOP Alters the Material Properties of Sclera and Lamina Cribrosa in Monkeys, Dis. Markers 2022 (2022) 5038847.
[68] R.E. Norman, J.G. Flanagan, I.A. Sigal, S.M. Rausch, I. Tertinegg, C.R. Ethier, Finite element modeling of the human sclera: influence on optic nerve head biomechanics and connections with glaucoma, Exp. Eye Res. 93 (1) (2011) 4–12.